Doppler-Resolved Spectroscopy as an Assignment Tool in the Spectrum of Singlet Methylene†

Gregory E. Hall,* Anatoly V. Komissarov, and Trevor J. Sears

Chemistry Department, Brookhaven National Laboratory, Upton, New York 11973-5000

Received: February 9, 2004; In Final Form: April 2, 2004

New spectra of methylene, CH_2, in the near-infrared have been obtained following 308 nm photolysis of ketene, CH_2CO. Nascent photofragment Doppler spectra and thermalization kinetics vary systematically with the energy of the absorbing level, providing additional information to support or refute spectroscopic assignments made on the basis of the frequency measurements and combination differences. New assignments in the 10800 cm^{-1} region extend to higher rotational levels than before and provide new spectroscopic term values for some CH_2 $\tilde{a}^1A_1$ state levels. The number and intensity distribution of unassigned lines in the spectrum is consistent with the expected transitions from vibrationally excited and high rotational levels of the $\tilde{a}^1A_1$ state and transitions due to $^{13}CH_2$ in natural abundance, and does not require a significant contribution from additional transitions arising from triplet-state perturbations.

1. Introduction

For the last 40 years, the visible spectrum of singlet methylene has been a proving ground for testing advances in our understanding of the high-resolution spectroscopy of small molecules. The $\tilde{b}^1B_1-\tilde{a}^1A_1$ band system in CH_2 is dominated by an irregular progression in the bending vibrational mode, extending from the near-infrared through the visible region of the spectrum. The two states involved form a Renner−Teller pair: both correlate with a degenerate $^1\Delta_g$ state at linearity. The ground, $\tilde{X}^3B_1$, state is 3150 cm^{-1} below the $\tilde{a}$ state, and perturbations caused by interactions among the three low-lying states result in an irregular absorption spectrum whose complete analysis has proved to be very difficult. Garcia-Moreno and Moore[1] summarized the spectroscopic work published before 1993, and our group has recently reported experimental work on the spectrum at longer wavelengths[2−4] where it is weaker, due to poorer Franck−Condon factors, but somewhat simpler, since the excited-state level density is reduced. Recent theoretical work by the Jensen[5] and Duxbury[6,7] groups has considerably advanced our understanding of the main features of the spectrum and the rovibronic interactions that account for its complexity.

However, despite the large volume of experimental and theoretical work devoted to its understanding, the observed spectrum at Doppler-limited resolution still contains many more absorption lines than have been assigned. In the visible region, Petek et al.[8,9] reported the measurement of approximately 10^4 lines in a 3000 cm^{-1} spectral region and could assign fewer than 500 of them. In the near-infrared, Kobayashi et al.[3,4] could assign nearly one-quarter of the observed lines, but the majority remained unassigned.

There are several sources of difficulty. The K_a-dependent mixing of $\tilde{a}$ and $\tilde{b}$ vibronic states gives dipole intensity to many zeroth-order vibrational overtone bands of the $\tilde{a}$ state that otherwise would have negligible intensity. The mixing also produces large deviations from asymmetric rigid rotor patterns in the $\tilde{b}$ state. This irregularity, combined with the wide spacing of rotational lines in multiple interleaved vibronic bands, confounds pattern recognition. Searching for lower state combination differences based on the rotational term values of Petek et al.[8,9] and supplemented by more recent work[1,3,10] has been the most secure path to new spectral assignments, although an unguided search produces an excessive number of coincidentally close, but mostly incorrect, possible assignments. Furthermore, many of the higher rotational energy levels in the $\tilde{a}$ state have not yet been spectroscopically identified. The large asymmetry of the $\tilde{a}$ state leads to relatively strong $\Delta K_a = 3$ subbands[11] in addition to those with $\Delta K_a = 1$. A few of the $\tilde{a}$ state levels are mixed with the triplet, $\tilde{X}^3B_1$, leading to doubling of some lines.[9,12] Triplet perturbations of the $\tilde{b}$ state might be expected to occur even more often due to the higher triplet density of vibrational states; indeed, about 60% of the assigned lines in the $\tilde{b} \leftarrow \tilde{a}$ spectrum between 540 and 640 nm showed magnetic activity,[8] which was originally attributed to pervasive mixing of $\tilde{b}$ and $\tilde{X}$ state levels.[8] However, subsequent analysis by Duxbury and Jungen[13] showed the qualitative patterns of magnetic activity could be explained by unpaired electronic angular momentum produced by the Renner−Teller interaction of the $\tilde{a}$ and $\tilde{b}$ states, without invoking mixing with the triplet $\tilde{X}$ state. Subsequently, a study of the variations in rovibronically resolved $\tilde{b}$ state radiative lifetimes was used to characterize the mixing with dark $\tilde{a}$ and $\tilde{X}$ state levels.[14] It was concluded that the dominant source of lengthened radiative lifetimes was Renner−Teller and Fermi interactions with the $\tilde{a}$ state, with additional random variations attributed to spin−orbit mixing with near-degenerate $\tilde{X}$ state levels. Many of the unassigned lines in the spectrum are undoubtedly caused by absorption from vibrationally excited $(\nu_1\nu_2\nu_3) = (010)$ $\tilde{a}^1A_1$ levels and higher rotational levels in the $\tilde{a}^1A_1(000)$ state, whose energies are presently not well-known. At the high dynamic range of the present experiments, one can also expect a contribution to the density of weaker lines due to $^{13}CH_2$ in natural abundance.

In the present work, we have recorded sections of the methylene spectrum in the $\tilde{b} \leftarrow \tilde{a}$ (020)−(000), (030)−(000), and (030)−(010) $K_a = 0-1$ subbands following 308 nm photodissociation of ketene under constant, low-pressure condi-

† Part of the special issue "Richard Bersohn Memorial Issue".

* To whom correspondence should be addressed. E-mail: gehall@bnl.gov.

10.1021/jp0494133 CCC: $27.50
Published on Web 05/08/2004

tions. The spectral region around 10800 cm^{-1} has not been previously recorded and analyzed, although many of the upper state level positions have been previously determined from work at other wavelengths.[2−4] The observed nascent line shapes and their thermalization kinetics are shown to vary systematically with the internal energy of the absorbing level, and hence provide considerable help in the identification of observed spectral features. The results are used to extend and correct some previous spectral assignments of these bands, while adding new spectroscopically accurate energies for a few ã state rotational levels. A related method of associating rovibronic transitions with the energy of the lower state has been reported by Green et al.[15] These authors collected laser-induced fluorescence scans for CH_2 at different ketene photodissociation wavelengths, chosen to vary the energy available for rotational excitation in CH_2 ã(000). In principle, a photofragment threshold excitation scan could provide an accurate energy for the initial state of any detected rotational line, although the process might be considered too tedious to be practical.

2. Experimental Details

CH_2 radicals were formed by 308 nm excimer laser photolysis of ketene, synthesized by the pyrolysis of acetic anhydride flowing past a hot filament (Osram-Sylvania air heater 016501). A key requirement for these systematic studies of pre-steady-state kinetics is to maintain a stable and reproducible flow of ketene and buffer gas at a total pressure low enough that thermalization occurs in a convenient time window, leading to distinctive kinetics for different CH_2 rotational states. For these measurements, a He−ketene mixture was prepared continuously and used immediately after unreacted anhydride and water were trapped in a dry ice cooled U tube. A 1 sccm flow of helium used as a carrier gas was bubbled through acetic anhydride at 0 °C via a sintered glass frit. With the filament turned off and the cold trap passing only He, the pumping speed was adjusted to maintain a pressure of 100 mTorr in the sample cell. The heater filament was then turned on and adjusted in temperature to maintain a constant total pressure of helium plus ketene of 200 mTorr in the absorption cell.

The He−ketene gas mixture was introduced through a series of pinholes along the length of a 1.5 m long absorption tube and pumped out through a central exit port using a throttle valve, liquid nitrogen trap, and mechanical pump. The photolysis and probe laser beams were aligned nearly coaxially through the cell, using 45° 308 nm reflecting, near-IR transmitting mirrors to combine and separate the UV and near-IR beams. The probe beam was reflected back for a second pass through the sample cell and then focused onto a fast silicon photodiode receiver. Details of the frequency-modulated absorption spectrometer used have been published previously.[16,17]

Spectra in the range between 10300 and 11500 cm^{-1} were measured using a Coherent MBR-110 cw Ti:sapphire probe laser, pumped by all lines of a Coherent Sabre argon ion laser. Undesired amplitude modulation of the probe laser at twice the dither frequency of an intracavity etalon produces a spurious 186 kHz background component in the demodulated transient signal. The size of the interfering signal was strongly wavelength dependent, arising from low-finesse etalon effects in the optical path, although stable in amplitude at a given wavelength. To minimize the problem, the 10 Hz firing of the photolysis excimer laser was phase locked to the 93 kHz etalon dither frequency and a background signal for subtraction was acquired with the photolysis laser blocked at every wavelength step during a scan. LabView programs developed in our laboratory controlled the data acquisition, archiving, and analysis. The data file for each scan (up to 30 GHz) typically consists of a series of 250-point transient differential absorption waveforms, spanning a 5 μs time window, acquired at probe frequencies separated by about 100 MHz, along with wavemeter frequency readout, laser power normalization channels, a second transient channel measured in quadrature for phase correction purposes,[17] and a background channel for noise subtraction. Spectra in the 12200 cm^{-1} region were recorded using a Coherent 899-29 Ti:sapphire ring laser, which did not require the background channel.

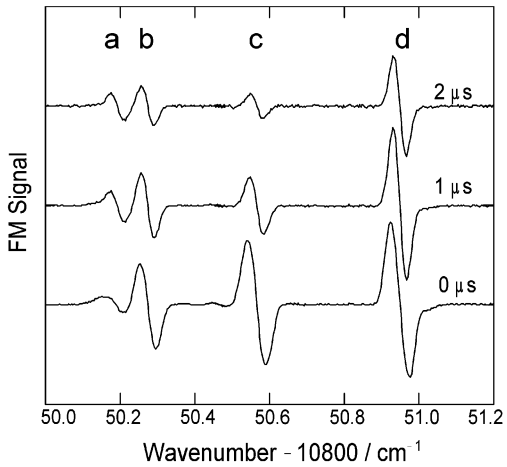

Figure 1. Selected time slices from the near-infrared transient FM spectrum of CH_2. The decay rates and nascent line widths vary widely among the observed rotational lines. The four strongest lines shown are (a) $4_{04}-3_{12}$ in the b̃(020)−ã(000) band, (b) unassigned line, likely originating in a low rotational state of ã(010), (c) unassigned line, likely originating in a high rotational state of ã(000), and (d) $4_{04}-4_{14}$ in the hot band b̃(030) −ã(010).

3. Results and Analysis

3.1. Doppler Widths and Thermalization Kinetics. We have recorded sections of the spectrum of CH_2 between 10538 and 11305 cm^{-1} under reproducible, low-pressure conditions, including a continuous region from 10779 to 10855 cm^{-1}. This region includes strong lines in the $\tilde{b}(020)^0-\tilde{a}(000)^1$ and $\tilde{b}(030)^0-\tilde{a}(010)^1$ subbands (the superscript is the K_a quantum number of the vibronic state). To confirm new assignments, we also recorded sections of the $\tilde{b}(030)^0-\tilde{a}(000)^1$ subband near 12200 cm^{-1}. This has been recorded previously,[18,19] but the present data are substantially higher quality and were recorded under the same low-pressure conditions as the longer wavelength data, to compare line shapes and decays. Figure 1 illustrates the variation in line widths and decay rates for a cluster of CH_2 rotational lines near 10850 cm^{-1}. One can clearly see that line c at 10850.55 cm^{-1} decays much faster than the others, and that the weaker, blended line a at 10850.19 is initially broader than the rest. Quantitative measurements of such nascent widths and decay rates for unassigned lines, when calibrated against the trends in assigned lines, provide additional information to support or refute tentative assignments of new lines. Lower state rotational level positions are known from the work of Petek et al.,[8] extended by our previous work,[3,4] and spectral assignments are made using lower state combination differences, complemented by the Doppler and kinetic measurements described below. New determinations of selected b̃ and ã state energy levels are summarized in Tables 1 and 2. A more extensive list of observed transition wavenumbers and intensities with partial assignments is available as Supporting Information.

TABLE 1: Selected $\tilde{b}^1B_1$ State Level Positions (cm^{-1})[a]

$J_{K_aK_c}$[b]	$(020)^0$ energy	$(030)^0$ energy	$J_{K_aK_c}$	$(010)^4$ energy
0_{00}	10826.989	12219.637		
1_{01}	10842.403	12235.147		
2_{02}	10873.233	12266.142	5_{41}	11460.905[c]
3_{03}	10919.495	12312.561	5_{42}	11460.921[c]
4_{04}	10980.844	12374.526		
	10982.179[c]			
5_{05}	11058.001	12452.104		
6_{06}	11150.307	12546.415[c]		
7_{07}	11257.959	12651.167[c]		
		12651.371[c]		
8_{08}	11380.833[c]	12775.004[c]		
9_{09}	11519.343[c]	12920.433[c]		

[a] Relative to the $\tilde{a}^1A_1(000)$ 0_{00} level. Estimated relative errors are less than 0.01 cm^{-1}, absolute error ± 0.02 cm^{-1}. [b] 4_{04} in (020) is observed to be split into two levels separated by 1.335 cm^{-1}, while 7_{07} in (030) is observed to be split by 0.204 cm^{-1}. [c] New or corrected value.

TABLE 2: Newly Determined $\tilde{a}^1A_1$ State Rotational Level Positions (cm^{-1})

$J_{K_aK_c}$	energy	$J_{K_aK_c}$	energy
8_{18} $(010)^a$	562.741	$9_{19}(000)^b$	699.287
$8_{17}(000)^b$	671.287	$9_{18}(000)^b$	819.841

[a] Relative to the $\tilde{a}^1A_1(010)$ 0_{00} level, which is 1352.45(2) cm^{-1} above the $\tilde{a}(000)$ 0_{00} level.[8] [b] Relative to the $\tilde{a}^1A_1(000)$ 0_{00} level. Estimated absolute errors ± 0.01 cm^{-1}.

The nascent state distribution of singlet CH_2 following photodissociation of ketene at a number of wavelengths has been characterized by the LIF experiments of Garcia-Moreno et al.[20,21] The rotational distributions of each vibrational state could be empirically described by a rotational temperature that varied smoothly with the excess energy above the dissociation threshold. Interpolating their results to a dissociation wavelength of 308 nm, the singlet CH_2 formed in the vibrational ground state can be characterized by a rotational temperature of about 800 K. About 25% of the singlet CH_2 is formed in the (010) vibrationally excited state with a rotational temperature of about 350 K. The yield of triplet CH_2 has been determined to be about 6% at this wavelength.[22]

Prior to thermalizing collisions, the velocity distribution of selected CH_2 states reflects the internal energy distribution of the coincident CO fragments. In a supersonic jet environment, the speed distribution can be inverted to estimate these coincident state distributions.[22,23] In a room temperature "bulb" experiment, the thermal parent velocity distribution limits the information that can be determined reliably by direct inversion, yet the mean translational energy can be extracted accurately from the nascent Doppler line shapes, providing a distinctive marker for the CH_2 state energy. Figure 2 illustrates the average translational energy derived from the nascent FM Doppler lines of assigned CH_2 states measured in the 10800 cm^{-1} region. Spectra were selected from a time window from 20 to 60 ns after the photolysis laser and fit with a two-parameter function to represent the center-of-mass velocity distribution: $x^a(1-x)^b$, with $x = v/v_{max}$. The empirical parameters a and b were used to generate a trial distribution for one of three identical Cartesian components of the velocity in the center-of-mass frame. For assigned transitions, v_{max} is fixed by energy and momentum conservation, and for unassigned lines, v_{max} is treated as a third adjustable parameter. The trial velocity distribution was numerically converted to a center-of-mass Doppler profile, and convolved with the room temperature velocity distribution of ketene to make a trial laboratory-frame Doppler line shape. Finally the FM line shape was computed from the finite differences at the sideband frequencies to compare to the phase-corrected experimental spectrum. Parameters a and b were adjusted for the best least-squares fit, and the average translational energy was derived from the second moment of the best-fit laboratory-frame absorption line shape. A simpler, Gaussian form provides accurate line shape and population fits for times greater that 1 μs, but systematically overestimates both the average translational energy and the populations at earlier times, when the line shapes are nonthermal.

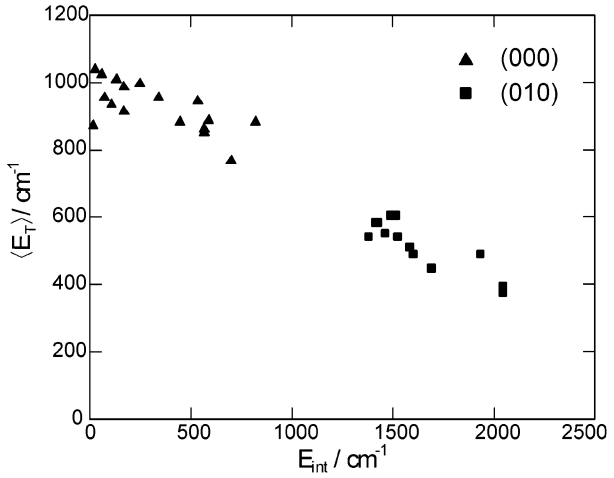

Figure 2. Average translational energy of singlet CH_2 states based on nonthermal fits to prompt FM Doppler spectra. The internal energy of the detected states includes the 1352 cm^{-1} vibrational energy for rotational levels in the (010) state.

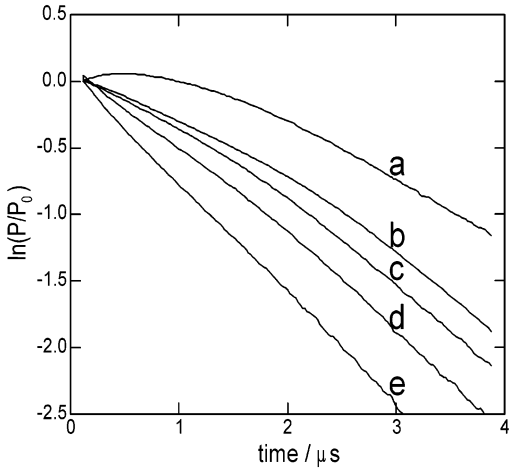

Figure 3. Normalized log decay plots of selected singlet CH_2 rotational state populations. The $J_{K_aK_c}$ quantum numbers for the illustrated states (in order of increasing rotational energy) are (a) 1_{10}, (b) 4_{14}, (c) 5_{15}, (d) 7_{17}, and (e) 9_{19}.

The first few collisions of nascent CH_2 with buffer gas and undissociated ketene smooth the CH_2 velocity distribution (and Doppler line shape) toward a Gaussian form, which then narrows as it approaches the bath temperature. The rotational distribution of CH_2 also relaxes from its initially hot distribution toward the bath temperature on a similar time scale. Meanwhile, the total population of singlet CH_2 is depleted by reaction with ketene and collision-induced intersystem crossing to the ground triplet state. The disappearance of the vibrationally excited $\tilde{a}$-(010) state is not appreciably faster than that of $\tilde{a}(000)$.[24] The Doppler-integrated intensity has been determined as a function of time from the same line shape fits described above for evaluating the initial average translational energy. Figure 3 shows the time-dependent populations for a series of rotational

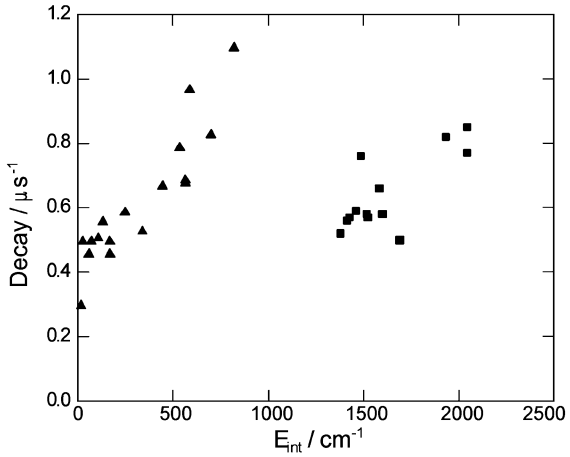

Figure 4. Decay rates during the 1−2 μs time window following ketene photolysis for selected CH_2 rotational levels in vibrational states (000) (triangles) and (010) (squares).

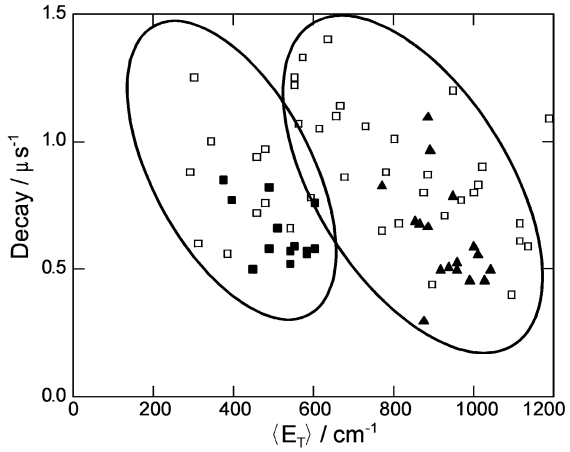

Figure 5. Correlation of nascent translational energy and thermalization/decay rates for assigned and unassigned CH_2 spectral lines. Assigned lines from rotational levels in the (010) state are solid squares in the left region. Assigned lines from rotational levels of the vibrational ground state (000) are solid triangles in the right region. Unassigned lines are shown as open squares.

levels in the vibrational ground $\tilde{a}(000)$ state. The logarithmic plots have been normalized at early times, and illustrate the systematic variation in decay kinetics with the rotational energy of the detected state. An arbitrary, but distinctive, attribute derived from such kinetic plots is the local slope of the logarithmic decay during the time interval from 1 to 2 μs after photolysis, when the rotational populations have not yet completely thermalized. Figure 4 shows the variation of this decay parameter with the internal energy of CH_2 states with assigned transitions in the present data set. Long-term stability and day-to-day reproducibility of the pyrolysis and flow conditions dominate the errors in these measurements, which occasionally differed by as much as 0.2 μs^{-1} in replicate runs on different days.

For lines in the experimental spectrum with relative intensities down to 0.005 of the most intense absorptions in the region, we are able to extract both translational energy and decay parameters. A correlation plot of these two parameters, as shown in Figure 5, provides a useful tool for identifying the vibrational and approximate rotational energy of the lower state involved in an unknown transition. The assigned lines originating in $v_2 = 0$ and $v_2 = 1$ (solid symbols) fall into two clusters, each dispersed according to rotational excitation. Within each cluster, denoted by the tilted ellipses, transitions from higher energy rotational states appear with faster decays and lower translational energies (up and to the left). Most of the unassigned lines (open symbols) can be confidently attributed to either cold- or hot-band transitions, and the rotational energy of the state responsible for the absorption can be estimated within a few hundred cm^{-1}. This additional information is often enough to refute a tentative assignment, or to suggest a preferable nearby candidate transition, subject to confirmation by combination differences. Making use of this behavior, we have been able to extend the spectral assignments in the regions studied. Table 1 lists some new or corrected rovibronic energies in the $\tilde{b}^1B_1$ state. A linked set of combination differences has also allowed us to determine several new spectroscopic term values for previously unknown rotational levels of $\tilde{a}^1A_1$ CH_2. These are summarized in Table 2.

3.2. Density of Spectral Lines and the Role of Triplet Perturbations in the $\tilde{b}$ State. Some considerable help in the assignment of the spectra also comes from theoretical calculations. For example, Jensen and co-workers[5] treat the Renner−Teller and anharmonic coupling between $\tilde{a}$ and $\tilde{b}$ state levels, and compute vibronic band origins that agree with experimental values within a few cm^{-1} for low K_a levels and within tens of cm^{-1} for higher K_a levels. A search through calculated line lists can provide a restricted, but still large, set of plausible assignments for the stronger lines. Even without complete assignments, however, some statistical properties of the unassigned lines can be profitably compared to calculated spectra to assess the extent of triplet mixing in the upper level.

The large dynamic range in the present data permits a comparison of the density and intensity distribution of lines in the observed spectrum with the calculations of Jensen and co-workers.[5,25] Since these calculations ignore the perturbations induced by spin−orbit mixing with background triplet levels, a comparison of the density and intensity distribution of lines with experimental spectra allows an independent test of the proposition[13] that strong perturbation of $\tilde{b}$ state levels by the dense $\tilde{X}$ state levels is infrequent, and that the pervasive magnetic activity of the $\tilde{b}$ state[8] is predominantly due to unquenched orbital angular momentum of the mixed $\tilde{a}$ and $\tilde{b}$ singlet states, unrelated to triplet perturbations.

For a 40 cm^{-1} section of spectrum starting at 10780 cm^{-1}, we sorted the measured absorption lines by nascent intensity and computed the cumulative density of lines as a function of threshold intensity. The results are plotted as the symbols in Figure 6, which illustrate, for example, that in this spectral region we find 0.3 line/cm^{-1} with an intensity at least 10% of that of the strongest line, and 1.6 lines/cm^{-1} with an intensity at least 1% of that of the strongest line. The upward curvature of this plot reflects an increasing number of *additional* weak lines detected for each constant factor of increased sensitivity. The line densities of the weaker lines should be considered lower limits, due to some blended weak lines that may not have been recognized. From asymmetries in the time-resolved Doppler-broadened FM spectra, pairs of lines separated by as little as 0.025 cm^{-1} (about half the room temperature Doppler width) are quite easy to recognize if the intensities differ by less than a factor of 10. We are confident in identifying nearly all the lines with intensities above 0.15% of that of the strongest line. Baseline noise levels with 20 shot averaging makes the counting of weaker lines less reliable.

The experimental distribution can be compared to calculations[5,25] of the frequencies and intensities for all transitions in this spectral region originating in levels up to $J = 10$ of $^{12}CH_2$ in the $\tilde{b}-\tilde{a}$ system. The calculated intensities were rescaled to

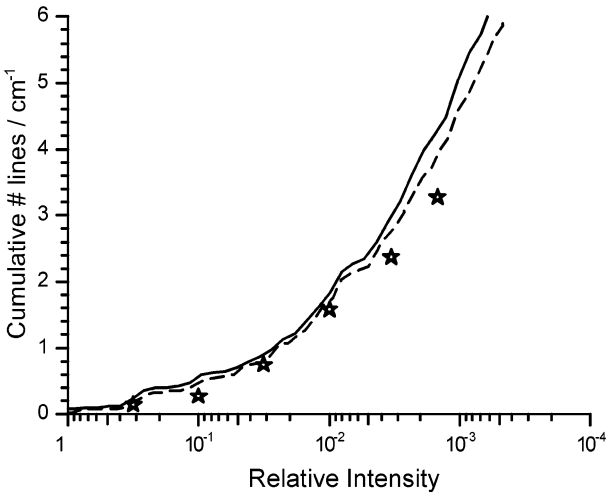

Figure 6. Spectral line density (lines/cm^{-1}) as a function of threshold intensity, relative to the strongest line. Symbols represent the observed line density in the 10800 cm^{-1} region. The dashed line is based on calculations of Jensen and co-workers.[5,25] The solid line includes a correction for triplet perturbations of the lower levels.

a rotational temperature of 800 K for the $\tilde{a}(000)$ level. We have included a separate contribution of calculated $^{13}CH_2$ transitions in this region, weighted by the 0.01 natural abundance. A set of lines tentatively assigned to the Q branch of the $\tilde{b}(020)^0-\tilde{a}(000)^1$ subband in $^{13}CH_2$ is observed 12−15 cm^{-1} to the red of the analogous $^{12}CH_2$ transitions. The intensities, kinetics, and line widths are consistent with this assignment, and the isotopic shift is consistent with unpublished calculations by Jensen.[25] We have not, however, systematically searched for other lines necessary to confirm the $^{13}CH_2$ assignments. A contribution to account for hot band transitions in the nascent spectrum was approximated using the experimental[21] vibrational branching ratio and rotational distribution to scale a frequency-offset copy of the calculated $\tilde{a}(000)$ transitions. Uncertainty in this hot band contribution probably dominates the error in the calculated intensity distribution. The resulting calculated intensity distribution is given by the dashed line in Figure 6, which agrees fairly well with the observations. The effects of spin−orbit mixing in the lower state have been estimated using a distribution of mixing coefficients similar to that computed by Bley and Temps.[26] A fraction of the original, unperturbed lines are replaced by pairs of lines, which share the original intensity according to the ratio of the corresponding mixing coefficients. The frequency and strength of triplet mixing in the $\tilde{a}(000)$ state should increase the density of weaker spectral lines as shown by the small change from the dashed to the solid line in Figure 6. Most of the extra lines with dominant triplet character are calculated to contribute to the line density only at still lower intensities. Triplet perturbations in the $\tilde{b}$ state would generate a further upward shift in the calculated line density, with a magnitude reflecting the relative frequency and strength of perturbations. The observed density of weak lines in this spectral region is no higher than that of the singlet calculations of Jensen,[5,25] implying that there is no need to invoke frequent strong triplet perturbations in the $\tilde{b}$ state to account for the observed density of spectral lines, at least in this spectral region and with a dynamic range of 1000:1. We must be clear that these observations cannot be taken as firm evidence against any triplet perturbations in the $\tilde{b}$ state, only that the perturbations within the singlet system are already complex enough to account for the observed density of weak lines.

Positive identification of instances of $\tilde{X}$ state mixing with the $\tilde{b}$ state is similarly lacking in the $\tilde{b}$ state radiative lifetime measurements by Garcia-Moreno et al.[14] When both members of a perturbed doublet were identified, neither line ever showed lifetimes as long as twice the unperturbed value. We take this as evidence that the perturbing state cannot be the triplet. Complete mixing with a dark state would double the lifetime of both components, and incomplete mixing would lead to a still longer lifetime for the doublet component with the larger dark state character. There are many instances of isolated perturbations within the singlet system that lead to a doubling of zeroth-order $\tilde{b}$ state rotational levels, where the perturbing level has enough $\tilde{b}$ state character to result in only modest lengthening of the radiative lifetime. Indeed, the rovibronically resolved transition moments calculated by Gu et al.[5,25] show J-dependent variations within different K_a states of selected vibronic levels. These small, apparently random fluctuations, as well as strong isolated doublings, arise in a detailed calculation of the Renner−Teller coupled singlet $\tilde{a}-\tilde{b}$ system. Additional couplings with the triplet likely occur, but will be difficult to identify unambiguously.

4. Conclusion

In a reversal of the usual roles of producer and consumer, we have applied some tools of photodissociation dynamics and kinetics to the solution of problems in spectroscopy. Following ultraviolet photodissociation of ketene, nascent photofragment Doppler profiles of unassigned rotational lines can be compared with those of known transitions to provide additional evidence to support or refute a trial assignment. When time-dependent spectra are collected with a reproducible flowing sample of ketene and inert gas, the kinetics of thermalization provide another characteristic marker of the rotational energy of the carrier state. Using these tools, we have extended and corrected some spectral assignments for CH_2 in the $\tilde{b}-\tilde{a}$ system.

Acknowledgment. This work was performed at Brookhaven National Laboratory under Contract No. DE_AC02_98CH10886 with the U.S. Department of Energy and supported by its Division of Chemical Sciences. We thank Prof. Per Jensen (Wuppertal) for providing us with a detailed list of calculated transition frequencies and intensities for $^{12}CH_2$ and $^{13}CH_2$ based on ref 5.

Supporting Information Available: Table containing observed CH_2 transitions and intensities (PDF). This material is available free of charge via the Internet at http://pubs.acs.org.

References and Notes

(1) Garcia-Moreno, I.; Moore, C. B. *J. Chem. Phys.* **1993**, *99*, 6429.
(2) Marr, A. J.; Sears, T. J.; Chang, B.-C. *J. Chem. Phys.* **1998**, *109*, 3431.
(3) Kobayashi, K.; Pride, L. D.; Sears, T. J. *J. Phys. Chem. A* **2000**, *104*, 10119.
(4) Kobayashi, K.; Sears, T. J. *Can. J. Phys.* **2001**, *79*, 347.
(5) Gu, J.-P.; Hirsch, G.; Buenker, R. J.; Brumm, M.; Osmann, G.; Bunker, P. R.; Jensen, P. *J. Mol. Struct.* **2000**, *517*−*8*, 247.
(6) Duxbury, G.; McDonald, B. D.; van Gough, M.; Alijah, A.; Jungen, C.; Paliva, H. *J. Chem. Phys.* **1998**, *108*, 2336.
(7) Duxbury, G.; Alijah, A.; McDonald, B. D.; Jungen, C. *J. Chem. Phys.* **1998**, *108*, 2351.
(8) Petek, H.; Nesbitt, D. J.; Darwin, D. C.; Moore, C. B. *J. Chem. Phys.* **1987**, *86*, 1172.
(9) Petek, H.; Nesbitt, D. J.; Moore, C. B.; Birss, F. W.; Ramsay, D. A. *J. Chem. Phys.* **1987**, *86*, 1189.

(10) Hartland, G. V.; Qin, D.; Dai, H.-L. *J. Chem. Phys.* **1995**, *102*, 6641.
(11) Hartland, G. V.; Xie, W.; Qin, D.; Dai, H.-L. *J. Chem. Phys.* **1992**, *97*, 7010.
(12) McKellar, A. R. W.; Bunker, P. R.; Sears, T. J.; Evenson, K. M.; Saykally, R. J.; Langhoff, S. R. *J. Chem. Phys.* **1983**, *79*, 5251.
(13) Duxbury, G.; Jungen, C. *Mol. Phys.* **1988**, *63*, 981.
(14) Garcia-Moreno, I.; Lovejoy, E. R.; Moore, C. B.; Duxbury, G. *J. Chem. Phys.* **1993**, *98*, 873.
(15) Green, W. H., Jr.; Chen, I.-C.; Bitto, H.; Guyer, D. R.; Moore, C. B. *J. Mol. Spectrosc.* **1989**, *138*, 614.
(16) Chang, B.-C.; Costen, M. L.; Marr, A. J.; Ritchie, G.; Hall, G. E.; Sears, T. J. *J. Mol. Spectrosc.* **2000**, *202*, 131.
(17) Hall, G. E.; North, S. W. *Annu. Rev. Phys. Chem.* **2000**, *51*, 243.
(18) Herzberg, G.; Johns, J. W. C. *Proc. R. Soc. London, Ser. A* **1966**, *295*, 107.
(19) Chang, B. C.; Wu, M.; Hall, G. E.; Sears, T. J. *J. Chem. Phys.* **1994**, *101*, 9236.
(20) Garcia-Moreno, I.; Lovejoy, E. R.; Moore, C. B. *J. Chem. Phys.* **1994**, *100*, 8890.
(21) Garcia-Moreno, I.; Lovejoy, E. R.; Moore, C. B. *J. Chem. Phys.* **1994**, *100*, 8902.
(22) Morgan, G. C.; Drabbels, M.; Wodtke, A. M. *J. Chem. Phys.* **1996**, *104*, 7460.
(23) Costen, M. L.; Katayanagi, H.; Hall, G. E. *J. Phys. Chem. A* **2000**, *104*, 10 247.
(24) Langford, A. O.; Petek, H.; Moore, C. B. *J. Chem. Phys.* **1983**, *78*, 6650.
(25) Jensen, P. Private communication, 2003.
(26) Bley, U.; Temps, F. *J. Chem. Phys.* **1993**, *98*, 1058.
(27) Bunker, P. R.; Jensen, P.; Kraemer, W. P.; Beardsworth, R. *J. Chem. Phys.* **1986**, *85*, 3724.